ARTICLE

High-Resolution Electron Microscopy Imaging of MOFs at Optimized Electron Dose

Received 00th January 20xx,
Accepted 00th January 20xx

DOI: 10.1039/x0xx00000x

Safiyye Kavak,[a] Daen Jannis,[a] Annick De Backer,[a] Daniel Arenas Esteban,[a] Arno Annys,[a] Sergio Carrasco,[b] Javier Ferrando-Ferrero,[b] Raúl M. Guerrero,[b] Patricia Horcajada,[b] Jo Verbeeck,[a] Sandra Van Aert,[a] Sara Bals,[a,*]

Local and high-resolution structural investigation of metal-organic frameworks (MOFs) is essential for understanding the role of defects and incorporated elements. In this paper, we characterize the structure of metalated versions of (Hf)PCN-222(H_2) and locate the position of the additional metal atoms. Transmission electron microscopy (TEM) is a powerful technique for this purpose, but MOFs are highly sensitive to the electron beam. To avoid structural alterations, it is therefore crucial to establish the maximum electron dose that can be applied. In this study, we apply a systematic workflow to measure the critical electron dose, enabling the identification of the optimal technique for extracting reliable information about the local structure of MOFs. We examined the electron beam stability of benchmarked (Zr)NU-1000, (Hf)PCN-222(H_2) and its metalated versions, (Hf)PCN-222(Fe) and (Hf)PCN-222(Pd), and identified factors influencing the stability under the electron beam. After the threshold for electron dose was established, we applied low-dose, four-dimensional scanning transmission electron microscopy (4D-STEM). We then compared annular bright field (ABF), annular dark field (ADF), and real-time integrated center of mass (riCOM) images that could be extracted from the 4D dataset. The riCOM technique successfully revealed the structure of investigated MOFs with minimal beam-induced alterations and provides insights into local features, including organic linkers and additional metalation elements.

Introduction

Metal-organic frameworks (MOFs) are fascinating hybrid materials comprised of metal ions/clusters and organic polycomplexant linkers, not just because of their high porosity and crystallinity but also because of their chemical, compositional, and structural versatilities.[1] Their excellent properties make them ideal candidates in various strategic fields such as catalysis,[2,3] controlled drug delivery,[4] energy storage devices,[5] and fluid storage and separation.[6,7] They allow for precise control over their size and morphology, facilitating the incorporation of additional functional blocks/moieties (*e.g.*, transition metal complexes to enhance the catalytic activity, intercalation of highly polarizing groups for gas storage/separation, etc.), merging with other functional materials in the form of composites, and introducing defects to boost their application properties.[8–10] Unraveling local features of MOFs, such as defects and incorporated elements, is crucial to understanding the properties of these materials. This level of characterization cannot be achieved through conventional techniques like X-ray powder diffraction (XRD) and Fourier-transform infrared spectroscopy (FTIR), which only provide average and bulk information. Raman spectroscopy is another valuable technique to study MOFs, offering the advantage of working under *in situ* conditions such as liquid environments.[11,12] However, this technique faces challenges such as interference from light sources with overlapping wavelengths, the sensitivity of the MOF to laser exposure, and providing spatial resolution at µm level.[12,13] Nuclear magnetic resonance (NMR) spectroscopy is another powerful tool for probing the chemical environment of atoms within MOFs. It can provide detailed information about the dynamics and interactions between the metal centers and organic linkers. Despite its strengths, NMR primarily offers averaged information and requires significant sample amounts, which can hide local heterogeneities and defects critical to the functionality of MOFs, still falling short of providing fully resolved spectra in MOFs.[14]

Transmission electron microscopy (TEM) is an excellent approach for localized investigation of MOFs. However, these materials are prone to damage under electron beam irradiation. Radiolysis is considered as the primary mechanism leading to beam damage in MOFs among other damage routes, including knock-on damage, charging, and heating.[15,16] As a result of electron beam damage, the organic linkers within the MOFs disintegrate, causing the system to undergo shrinkage.[17] To mitigate beam damage and to increase the imaging lifetime of MOFs under the electron beam, cryo-TEM was previously used.[18] Although cryogenic experiments indeed help to increase the stability of MOFs in the TEM by 3-4 times,[19] they do not offer sufficient insight concerning the behavior of the materials during actual working conditions, which typically involve higher temperatures. Therefore, alternative methods to image MOFs, while

[a] *Electron Microscopy for Materials Science (EMAT), University of Antwerp, Groenenborgerlaan 171, 2020 Antwerp, Belgium.E-mail: Sara.Bals@uantwerpen.be*
[b] *Advanced Porous Materials Unit, IMDEA Energy Institute, Móstoles, 28935 Madrid, Spain.*

† Supplementary Information available: [details of any supplementary information available should be included here]. See DOI: 10.1039/x0xx00000x

avoiding electron beam damage should be developed. Previously, it was shown that the use of direct-detection electron counting (DDEC) cameras,[20–22] integrated differential phase contrast (iDPC) imaging,[15,23–26] and four-dimensional scanning transmission electron microscopy (4D-STEM)[27,28] based techniques are very useful approaches to characterize beam-sensitive materials.[19] Important hereby is a quantitative approach to estimate the accumulated electron dose or "critical dose" that can be applied to a specific MOF crystal without degradation of the structure.[29,30] Indeed, the degradation behavior varies for each type of MOF, with critical electron doses reported at around 25 $e^{-}Å^{-2}$ for the zinc(II) imidazolate ZIF-8, indicating the initiation of crystallinity loss, whereas the zirconium(IV) tetracarboxylate (Zr)NU-1000 and the chromium(III) dicarboxylate MIL-101(Cr) demonstrate preservation of their structure even at doses above 100 $e^{-}Å^{-2}$.[15,31] The MOF stability is generally determined by the strength of the coordination bonds, following the hard and soft acids and bases (HSAB) principle and depending on the nature of the metals and polydentate organic linkers (*i.e.* hard metals, Cr^{3+}, Zr^{4+}, form stable bonds with hard linkers-carboxylates, and soft metals, Zn^{2+}, with soft ligands-nitrogenated linkers).[32] However, the sensitivity of the MOF may also be affected by particle size, type of metal clusters, linker connectivity, and guest molecules, among others.[33,34]

In this study, we apply a systematic workflow to measure the critical electron dose, enabling the identification of the optimal technique for extracting reliable information about the local structure of MOFs. By integrating advanced imaging methods with precise dose measurements, our approach enables high-resolution structural analysis while effectively minimizing beam-induced alterations. To confirm the accuracy of the methodology, we first investigated (Zr)NU-1000 (NU, Northwestern University) with known electron beam stability.[15] Then, to demonstrate the applicability of the approach, we further investigated the PCN-222 (PCN, porous coordination network), which is composed of hafnium and tetrakis(4-carboxyphenyl)porphyrin (hereinafter, TCPP).

Notably, PCN-222 finds widespread application in catalysis and is recognized for its chemical stability in a wide variety of harsh conditions, even after long periods of time.[35,36] Metalation of the porphyrin linker, resulting in metalated PCN-222, denoted as (Hf)PCN-222(M), allows for the insertion of additional cations in the structure, particularly in the center of the polypyrrole ring of the porphyrin. This leads to improved catalytic properties, such as photoreduction of CO_2,[37] and cycloaddition reactions.[38] The additional metal atoms are expected to be present at the center of the porphyrin linker[39] or, as suggested by other authors, slightly shifted out of the central plane, when coordinated to other counterions such as Cl.[40,41] However, to the best of our knowledge, the position of these atoms has never been visualized by high-resolution electron microscopy. In doing so, it is important to avoid the electron beam changing the structure; therefore, knowledge of the critical dose is essential. The fact of identifying the position of these additional cations in the structure has been claimed as critical in order to offer a realistic explanation regarding the significant outcomes in different catalytic reactions, depending on the nature of the metal cation and its axial coordination.[42] For instance, catalytic cycles transit through the formation of a planar transition state complex in the case of Ni- and Cu-based porphyrins according to their preferential coordination environment, which turns them into excellent catalysts in Diels-Alder cycloadditions.[43,44] However, they are poor catalysts in CO_2 fixation as the square pyramid conformation is not typically stabilized, contrary to Co- and Zn-based porphyrins, which are excellent catalysts for CO_2 conversion into high-added value products, but inactive in pericyclic reactions.[38] These differences reflect the need to measure and locate the metal cations within MOF structures accurately.

The structure of the paper is as follows: first, we investigated the beam stability of (Zr)NU-1000 and measured the critical dose to confirm the accuracy of the methodology. Next, we applied a dedicated approach to measure the electron beam stability of pristine, non-metalated, (Hf)PCN-222(H_2). To further understand the factors that influence the MOF degradation/stabilization, we then investigated two metalated versions of the sample: (Hf)PCN-222(Fe) and (Hf)PCN-222(Pd). Moreover, we characterized (Hf)PCN-222(Fe) particles with two different sizes and/or elemental ratios. Based on our assessment of the electron dose that can be applied with minimal structural degradation, we identified the optimal electron dose to thoroughly investigate high-resolution structural details, including the positioning of metalation atoms. This was achieved by conducting 4D-STEM experiments and using the real-time integrated center of mass (riCOM)[45] algorithm, enabling high-resolution imaging while minimizing structural degradation caused by the electron dose.

Methods

Synthesis Procedure

(Zr)NU-1000, (Hf)PCN-222(H_2), (Hf)PCN-222(Pd), (Hf)PCN-222(Fe)-L, and (Hf)PCN-222(Fe)-S were synthesized according to previously reported protocols,[38,46–48] that have been modified to obtain the MOFs in the convenient particle size. Further details on the synthesis procedures can be found in the SI.

High-angle annular dark-field scanning transmission electron microscopy (HAADF-STEM) imaging, energy dispersion X-ray spectroscopy (EDX) measurements, and electron tomography

For all electron microscopy experiments, samples were drop-cast on a carbon-coated copper grid. An aberration-corrected Thermo Fisher Scientific Titan^3 electron microscope operating at 300 kV was used. Specific experimental parameters are given in the SI.

Particle dimensions were measured from high-angle annular dark-field scanning transmission electron microscopy (HAADF-STEM) overview images (Fig. SI.1). The average particle length, width, and aspect ratio distributions for each sample are presented in Table 1. The average metal amounts from energy dispersion X-ray spectroscopy (EDX) analysis for each sample are summarized in Table 2. Detailed information on HAADF-STEM, electron tomography, EDX, and electron beam stability of all samples presented in the corresponding sections of the SI.

Table 1. Average length, width, and aspect ratio for all samples together with their standard errors. (Please refer to the Supplementary Information for the details.)

	length (nm)	width (nm)	aspect ratio (width/length)
(Zr)NU-1000	898 ± 14	276 ± 4	0.31 ± 0.00
(Hf)PCN-222(H2)	610 ± 6	210 ± 3	0.35 ± 0.01
(Hf)PCN-222(Pd)	410 ± 6	156 ± 2	0.39 ± 0.00
(Hf)PCN-222(Fe)-L	467 ± 7	85 ± 1	0.19 ± 0.00
(Hf)PCN-222(Fe)-S	88 ± 1	43 ± 1	0.48 ± 0.00

Table 2. Average metal amounts in samples in atomic percentages with their errors (from the metal cluster of MOF, and the additional metalation). (Please refer to the Supplementary Information for the details.)

	metal cluster type of MOF (at.%)		metalation metal type (at.%)	
	Hf	Zr	Fe	Pd
(Zr)NU-1000		1.47 ± 0.19		
(Hf)PCN-222(H_2)	2.27 ± 0.25			
(Hf)PCN-222(Pd)	1.17 ± 0.15			0.42 ± 0.06
(Hf)PCN-222(Fe)-L	1.58 ± 0.17		0.76 ± 0.11	
(Hf)PCN-222(Fe)-S	0.68 ± 0.08		0.17 ± 0.03	

Electron beam stability calculations

Electron beam stability measurements were performed by acquiring a time series of HAADF-STEM images. To accurately calculate the applied beam current, a calibration curve, considering the monochromator excitation values and the screen current, was defined for every experiment. The electron dose, *D*, is calculated in terms of e^{-}Å^{-2} by the following equation:

$$D = \frac{I \times t}{e \times p^2} \quad (1)$$

where *I* is the beam current in amperes (A), *t* is the dwell time in seconds (s), *e* is the elementary charge of an electron (1.602x10^{-19} Coulombs per electron), and *p* is pixel size in angstrom (Å).

We would like to emphasize that a previous study, in which the same microscope and direct electron detector (Timepix3) was used[49] concluded that the uncertainty in extrapolated measurements from the fluorescent screen was approximately 10%. Importantly, this approach using a direct electron detector can be applied to any microscope, enabling accurate extrapolated measurements of the fluorescent screen current. For non-monochromated microscopes and without access to direct electron detectors, accurate beam current measurements can be achieved using a Faraday cup and an external amperemeter.[50]

To investigate the effect of electron dose rate, which is the electron dose per unit of time, electron beam currents of 0.5, 1, and 3 pA were applied, while keeping the dwell time and the pixel size constant at 2 µs and 101.7 pm, respectively. These parameters resulted in electron dose rates of 0.6, 1.2, and 3.6 e^{-}Å^{-2}s^{-1}. A dwell time of 2 µs, resulted in a frame time of 10.4 s for an image size of 2048 x 2048. To compare the effect of dose rate while keeping the accumulated dose the same, 320, 160, and 55 frames were acquired with dose rates of 0.6, 1.2, and 3.6 e^{-}Å^{-2}s^{-1}, respectively.

To investigate the beam stability, previous studies made use of selected area diffraction patterns.[30,51] In the current work, our final aim was to image the real space structure of the MOF using STEM, for which a focused probe is used. Therefore, we opted to calculate the diffractograms (obtained by Fourier transforming a subset of the recorded HAADF images) rather than collecting selected area diffraction patterns for which a parallel beam is applied. A similar study was conducted by Haase et al. to quantitatively compare the electron beam stabilities of covalent-organic frameworks (COFs).[29] As a measure for structural changes induced by the electron beam, changes in the intensity of diffractogram spots and/or the position of the diffractogram spots can be investigated. In our experiments, we observed that certain particles were rotating when exposed to the beam (Supplementary Movie 5,6). Despite the overall decrease in the diffractogram intensities, particle rotation results in an increase in diffractogram intensities when the particles align along a specific zone axis orientation. On the other hand, the distance between diffractogram spots remains unaffected during rotation, so we here focused on quantifying this distance, which corresponds to a change in the *d*-spacing of the lattice planes in the MOF. We typically observed this distance to increase with increasing dose. An increase in the distance between diffractogram spots corresponds to a decrease in *d*-spacing and therefore collapse or shrinkage of the MOF in real space. To measure the change in d-space in the diffractograms, we used the TrackMate tool, implemented in the ImageJ software.[52,53] Next, the *d*-spacing values were normalized by dividing every value by the maximum *d*-spacing that was measured at the beginning of the experiment (*d*-spacing$_{max}$). Since the main damage mechanism in MOFs is radiolysis,[15,16] and since radiolysis exhibits first-order decay characteristics[54], a first-order exponential decay function:

$$y_0 + Ae^{-D/D_c} \quad (2)$$

was fitted to the normalized *d*-spacing values as a function of total electron dose, with *D* the total electron dose, y_0 the final (steady-state) value the system reaches, *A* the amplitude representing the extent of variations, and D_c the critical electron dose, which is defined as the value for which the normalized *d*-spacing value decreased to 1/e (~0.37). The total half-life time electron dose $D_{1/2}$ where half of the total change occurred, can be calculated as D_c*ln(2). In our investigation, we considered $D_{1/2}$ as a key parameter to assess and compare the beam stability of different samples. The initial time to focus the particle before stability measurements was limited as much as possible. For measurements with a beam current exceeding 1 pA (dose rate higher than 1.2 e^{-}Å^{-2}s^{-1}), we performed an initial focusing step at lower magnification by using a beam current of no more than 1 pA to minimize beam damage prior to data acquisition. Subsequently, we immediately blanked the beam, adjusted the parameters to have the desired beam current and

magnification, and then unblanked the beam to start data acquisition.

riCOM (real-time integrated center of mass) imaging[45]

Once the critical dose was determined, we characterized the MOF structure under low-dose conditions by performing 4D-STEM experiments. During such experiments, a pixelated detector is employed to capture convergent beam electron diffraction (CBED) patterns at every probe position. By scanning the beam over the specimen in 2D and recording 2D CBED data for every scan position, a 4D data set is generated.[55] 4D-STEM data sets enable the generation of diverse images such as ptychography,[56,57] integrated differential phase contrast (iDPC) or integrated center-of-mass (iCOM),[26,45,58] using virtual detectors and algorithms. Here, 4D-STEM was used to retrieve the iCOM signal, which is approximately linearly dependent on the projected electrostatic potential of the specimen and has a better signal-to-noise ratio compared to conventional methods based on annular detectors.[59] In this work, the riCOM algorithm was applied,[45] which is a real-time reconstruction method that uses a kernel-based approach to create high-quality images with low computational requirements. We opted for the riCOM approach because it offers quasi real-time monitoring capabilities. In comparison, ptychography requires specific parameter tuning and involves significant computational time, while iDPC is merely a practical approximation of iCOM.[58] Further details on 4D-STEM imaging can be found in the SI.

Results and discussion

Electron beam stability measurements

To ensure the accuracy of the methodology that we applied to measure the critical electron dose, we first used the approach explained in the Methods section to quantify the electron beam

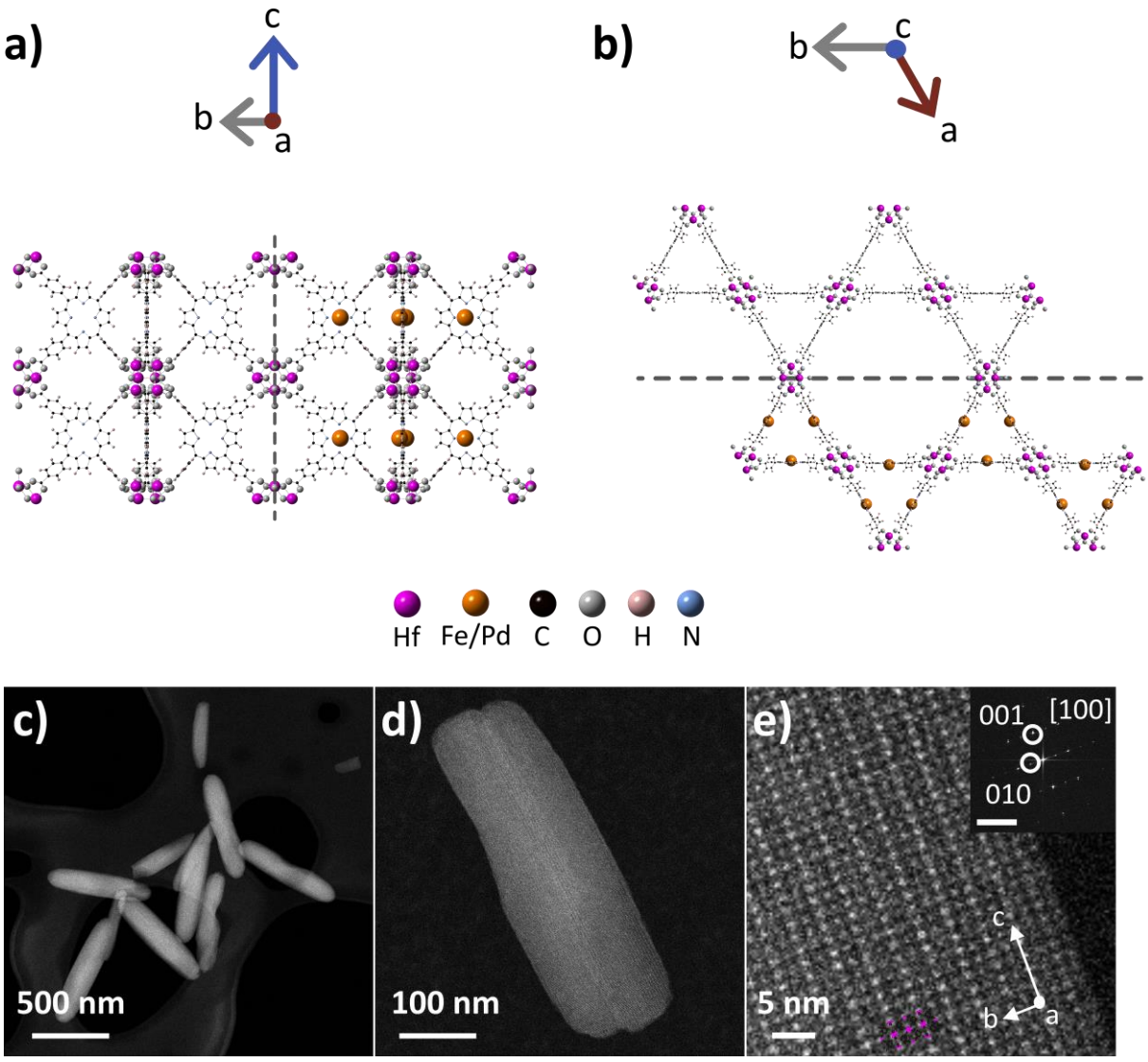

Fig. 1. Crystal structure of (Hf)PCN-222 along the a and b directions (**a**), and the c-direction (**b**) in the presence or absence of additional metalation elements. Color code is given inside the figure with corresponding elements at the expected positions. The constitutive metals of MOF (Hf, magenta spheres), and the additional metalation elements (Fe/Pd, orange spheres) are displayed larger for clear visualization. HAADF-STEM images of (Hf)PCN-222(H_2) particles at low magnification (**c**, **d**), and higher magnification along the [100] zone axis (**e**). The lattice direction is indicated within the image, and the theoretical structure is superimposed for comparison. The inset in (**e**) displays the diffractogram of the image, highlighting corresponding reflections, with a scale bar corresponding to 1 nm^{-1}.

stability of a well-known MOF, (Zr)NU-1000, with a crystal structure similar to (Hf)PCN-222(H_2). It was previously reported that the (Zr)NU-1000 starts to shrink even at doses below 10 $e^-Å^{-2}$, but the porous structure can be maintained even above 100 $e^-Å^{-2}$.[15] We here investigated the (Zr)NU-1000 electron beam stability by applying a dose rate of 1.2 $e^-Å^{-2}s^{-1}$. A decrease in *d*-spacing, in other words shrinking, from its diffractogram was already observed for the first frame (~10 $e^-Å^{-2}$) and $D_{1/2}$ was found to be equal to 202.40 $e^-Å^{-2}$ (Fig. SI.6 and Table SI.2), which is consistent with the findings reported in the literature.[15] This agreement demonstrates the applicability of our approach.

Next, we focused on pristine (Hf)PCN-222(H_2), a MOF for which the electron beam stability is unknown and which is the main sample of interest in this study. Fig. 1 (a-b) illustrates the crystal structure of (Hf)PCN-222(H_2) imaged along primary zone axes, revealing one-dimensional channels with a diameter of approximately 3.7 nm oriented according to the c-axis (Fig. 1. b). The HAADF-STEM images, captured at low and high magnifications, illustrate the overall particle morphology and the crystal structure (Fig. 1. c-e).

To investigate the degradation behavior, a time series of HAADF-STEM images was acquired for a given particle with an electron dose rate of 3.6 $e^-Å^{-2}s^{-1}$ (Fig. 2. a-b). The intensity of the diffractogram spots corresponding to the (001) reflections was found to decrease (see Method section for details indicating sample degradation). Moreover, the diffractogram peaks were observed to shift to higher values (nm^{-1}) with increasing accumulated dose (Fig. 2. c). Fig. 2.d shows that the d_{001}-spacing (nm) decreased, which indicates shrinkage of the MOF. An exponential curve was fitted to the normalized *d*-spacing of (Hf)PCN-222(H_2) and the electron dose to reach half-life time, $D_{1/2}$, was calculated.

The experiment was repeated by applying different electron dose rates (Fig. 3) (Please refer to Fig. SI.11 for the decay curves

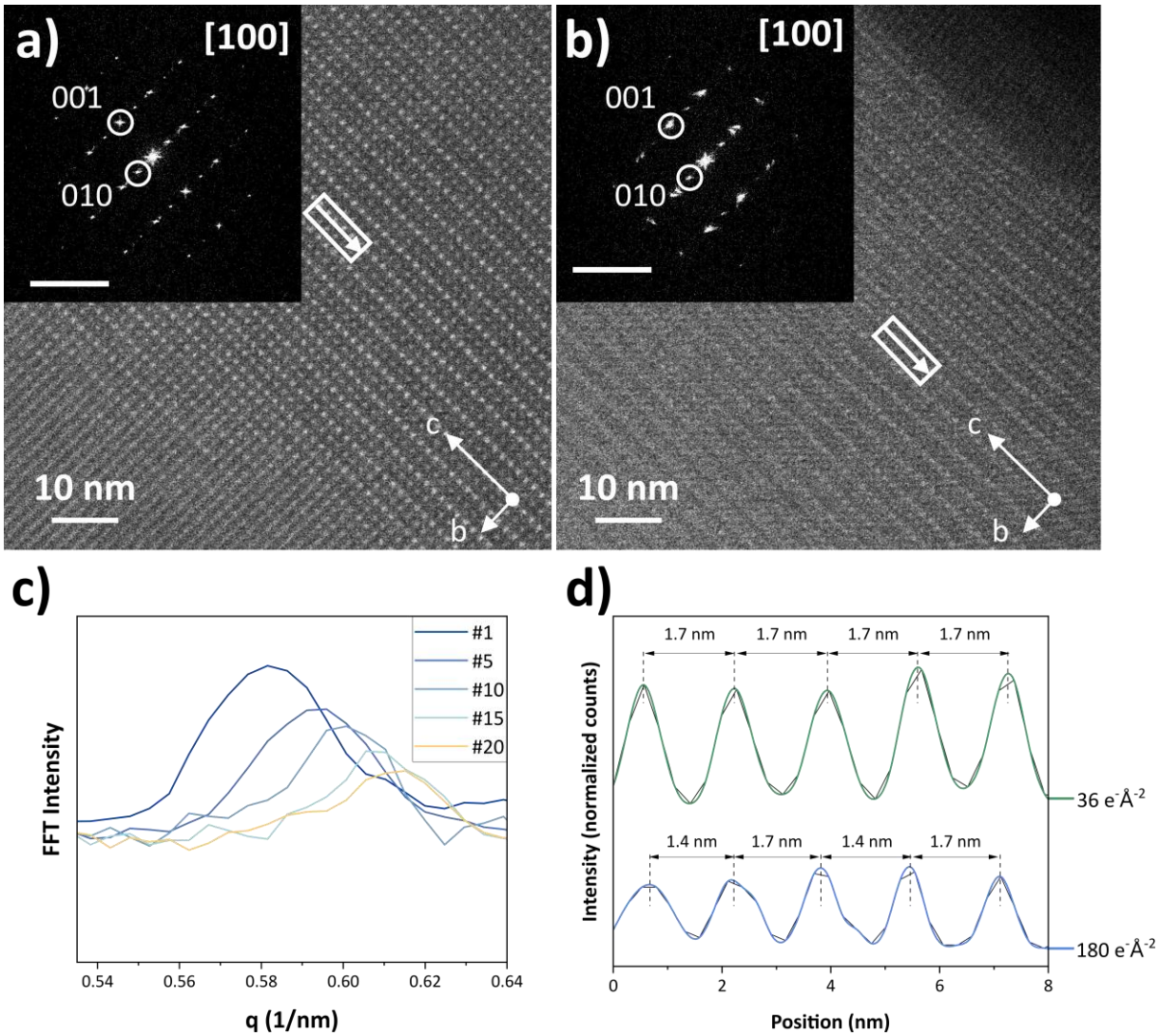

Fig. 2 HAADF-STEM images of (Hf)PCN-222(H_2) acquired with total electron doses of 36 (**a**), and 180 (**b**) $e^-Å^{-2}$ at an electron dose rate of 3.6 $e^-Å^{-2}s^{-1}$. The lattice directions are indicated within the images (**a**, **b**). Insets show diffractograms of the corresponding images, with scale bars representing 1 nm^{-1}, and with corresponding reflections. The distance between two (001) reflection spots in the diffractograms, is 1.17 nm^{-1} (**a**) and 1.26 nm^{-1} (**b**) which correspond to *d*-spacings of 1.71 nm (**a**) and 1.59 nm (**b**). The (001) reflections in the diffractogram are found to broaden and shift as a function of accumulated dose. The different curves correspond to different frames and therefore increasing accumulated electron dose (**c**). Normalized *d*-spacings indicate shrinking of the pores (**d**), with the corresponing locations of intensity profiles highlighted by rectangled arrows in the images (a, b). In the graph, the thinner black line represents the original data points, while the colored lines represent smoothed data for enhanced quantification.

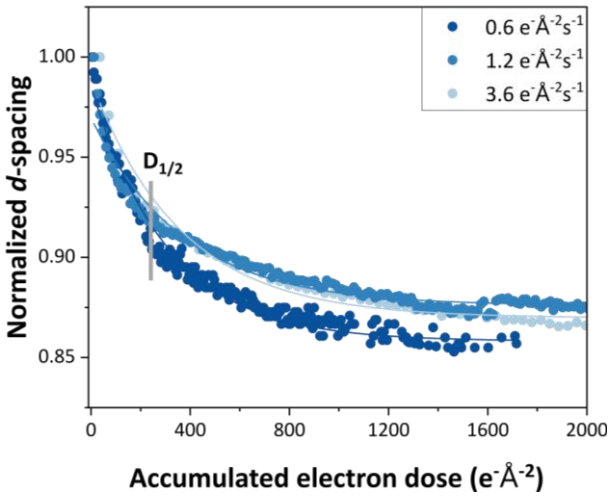

Fig. 3 Electron beam stability data and exponential decay curves of (Hf)PCN-222(H_2) by applying dose rates of 0.6, 1.2, and 3.6 $e^-Å^{-2}s^{-1}$ (see the Supplementary Information for more data). The straight lines represent the exponential fits to the corresponding data set. The vertical line represents the average $D_{1/2}$ values of corresponding dose rates.

of all beam stability experiments on (Hf)PCN-222(H_2) at all dose rates, and Table SI.4 for the fitted parameters of these experiments). Average values of $D_{1/2}$, the mean half-life time electron dose calculated across multiple particles, of (Hf)PCN-222(H_2) were found to be equal to 245 ± 5, 242 ± 9, and 254 ± 18 $e^-Å^{-2}$ for electron dose rates of 0.6, 1.2, and 3.6 $e^-Å^{-2}s^{-1}$, respectively (Table 3 and SI.4). The average $D_{1/2}$ values from different dose rates overlap within the range of their respective errors. Our results indicate that the dose rate had a minimal impact on the $D_{1/2}$ value for (Hf)PCN-222(H_2) and that the total electron dose, rather than the dose rate, is the primary factor influencing the beam damage of (Hf)PCN-222(H_2).

To evaluate the effect of metalation on electron beam stability, the experiments described above were repeated for (Hf)PCN-222(Pd). Hereby, "metalation" refers to additionally introduced metal elements inside the (Hf)PCN-222 structure, as previously illustrated in Fig. 1 (a-b). Electron beam stability measurements for (Hf)PCN-222(Pd) (Fig. SI.17 and Table SI.6) were performed with electron dose rates of 0.6, 1.2 and 3.6 $e^-Å^{-2}s^{-1}$. Again, $D_{1/2}$ was calculated from their exponential decay curves and compared to pristine (Hf)PCN-222(H_2) at all dose rates, as presented in Fig. 4. Fig. 4 shows that the metalated version of (Hf)PCN-222(H_2), *i.e.* (Hf)PCN-222(Pd), exhibits a smaller overall change in *d*-spacing compared to (Hf)PCN-222(H_2) at all dose rates. The metalated version, (Hf)PCN-222(Pd), showed an overall change in *d*-spacing of approximately 10% at all dose rates, as calculated from the experimental measurements, whereas a change of around 14% was found for pristine

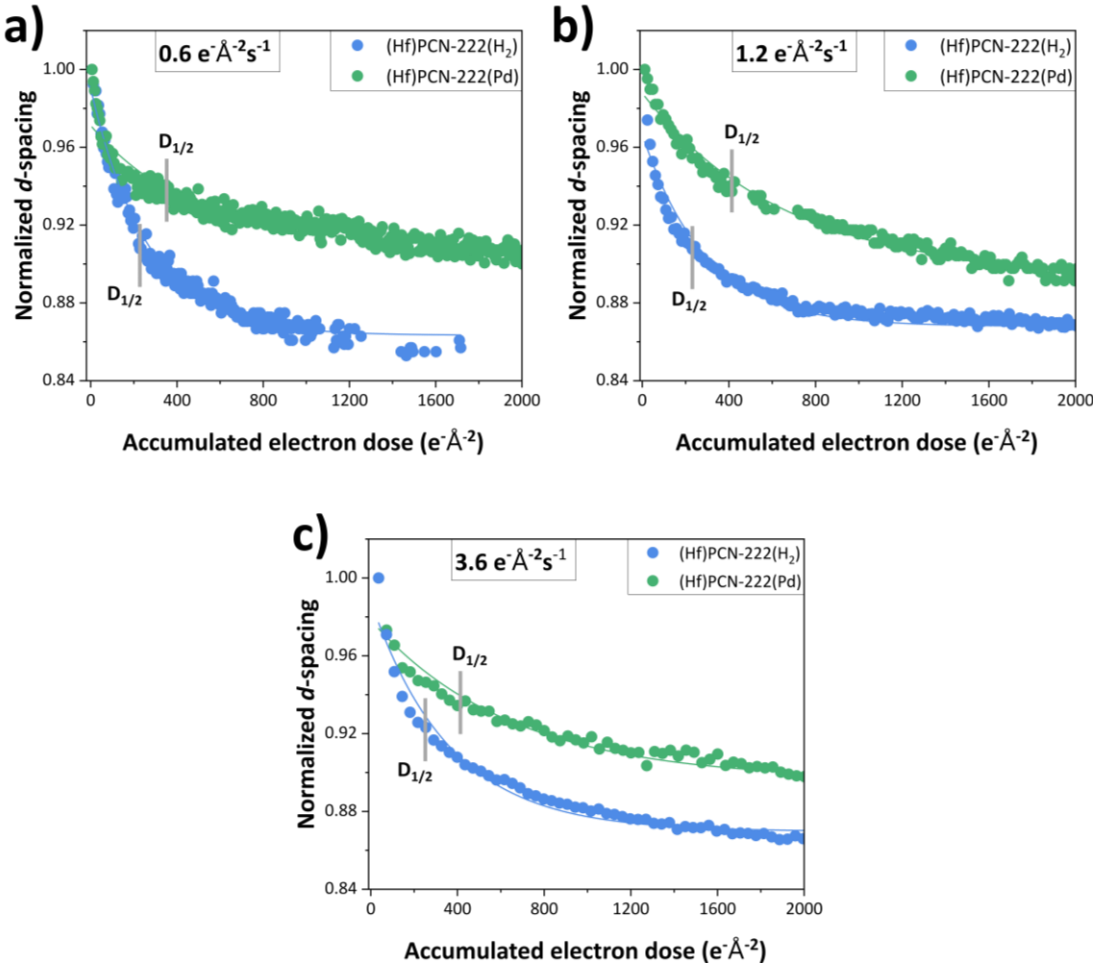

Fig. 4 Electron beam stability data and exponential decay curves of (Hf)PCN-222(H_2) (blue), and its metalated version: (Hf)PCN-222(Pd) (green) by using a dose rate of 0.6 (**a**), 1.2 (**b**), and 3.6 $e^-Å^{-2}s^{-1}$ (**c**).

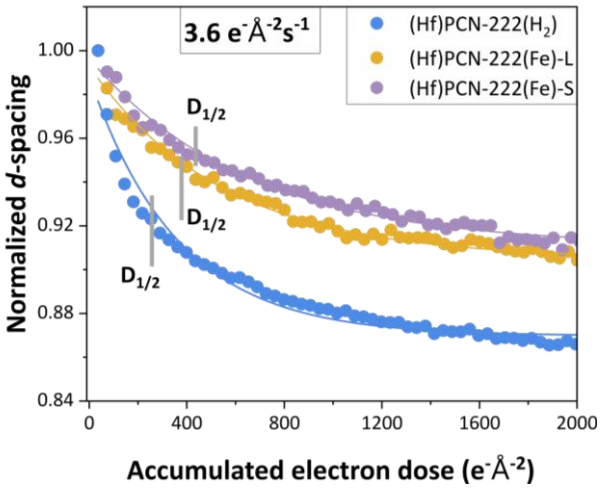

Fig. 5 Comparison of exponential decay curves of (Hf)PCN-222(H_2), (Hf)PCN-222(Fe)-L, and (Hf)PCN-222(Fe)-S by using 3.6 $e^-Å^{-2}s^{-1}$. The straight lines represent the exponential fits of the corresponding data set. The dashed vertical lines represent the average $D_{1/2}$ values for the corresponding samples.

(Hf)PCN-222(H_2). The metalated MOF also exhibits higher $D_{1/2}$ values in comparison to (Hf)PCN-222(H_2) for every dose rate. Our findings indicate the importance of evaluating the electron beam stability depending on the precise composition of the MOF. Especially for samples as sensitive to the electron beam as MOFs, such insights are extremely valuable since "every electron counts". Moreover, our results highlight the metalation as a route to significantly enhance the electron beam stability of MOF, potentially by a factor of 2. Previous studies have highlighted the loss of H atoms as a critical factor contributing to radiation beam damage.[60] It has been demonstrated that the electron beam stability of phthalocyanine increases with Cu-phthalocyanine, where H atoms inside the phthalocyanine replaced by Cu atoms, and becomes even more stable with chlorinated Cu-phthalocyanine since the structure became less prone to displacement compared to H.[60,61] In our system, the replacement of H_2 with Fe or Pd inside the porphyrin ring enhanced the stability under electron beam. It was already known that, from a synthetic and structural point of view, metalated PCNs are considerably more stable than their non-metalated counterparts.[62] In fact, the first report on porphyrin-based MOFs mentioned that, from a synthetic point of view, preparing the metalated version of the materials is much easier, resulting in improved crystallinity and yield.[36] The presence of the metal cation within the porphyrin enhanced the acidity of the coordinating carboxylic acid moieties, resulting in stronger coordination bonds, so more stable products. However, until now, this behavior has not been extended to the study of MOF stability under electron beam irradiation.

In contrast to (Hf)PCN-222(H_2), for which $D_{1/2}$ stayed similar for all dose rates, the $D_{1/2}$ value for (Hf)PCN-222(Pd) slightly increased from 329 ± 11 $e^-Å^{-2}$ to 396 ± 16 $e^-Å^{-2}$ with an increasing dose rate from 0.6 $e^-Å^{-2}s^{-1}$ to 1.2 $e^-Å^{-2}s^{-1}$ (Table 3, SI.8). However, as the dose rate increases from 1.2 to 3.6 $e^-Å^{-2}s^{-1}$, the $D_{1/2}$ values of 396 ± 16, and 400 ± 21 $e^-Å^{-2}$, respectively, cannot be distinguished. These findings again indicate that rather than the dose rate, total electron dose has a critical effect on the beam damage mechanism during STEM for (Hf)PCN-222(H_2) and its metalated version, (Hf)PCN-222(Pd)).[63,64]

Next, we investigated the effect of particle size and metal amount on the electron beam stability. Two different samples notated as (Hf)PCN-222(Fe)-L, and (Hf)PCN-222(Fe)-S were synthesized as explained in the methods section but resulted in structural differences. As presented in Table 1, (Hf)PCN-222(Fe)-S had a much smaller average length and width than those of (Hf)PCN-222(Fe)-L. These MOFs did not only differ in dimensions but also in metal amounts. As shown in Table 2, EDX analysis revealed that (Hf)PCN-222(Fe)-L exhibited average concentrations of 0.76 at.% for Fe and 1.58 at.% for Hf, resulting in a Fe/Hf ratio of 0.48. On the other hand, (Hf)PCN-222(Fe)-S showed average concentrations of 0.16 at.% for Fe and 0.68 at.% for Hf, resulting in a Fe/Hf ratio of 0.24. These results are in good agreement with those found in elemental analysis (ICP-OES, Table SI.11: see section 3 in SI).

The electron beam stabilities were measured by applying a dose rate of 3.6 $e^-Å^{-2}s^{-1}$ to (Hf)PCN-222(Fe)-L (Fig. SI.23, Table SI.8), and (Hf)PCN-222(Fe)-S (Fig. SI.29, Table SI.10). As given in Fig. 5, both (Hf)PCN-222(Fe) samples have higher $D_{1/2}$ in comparison to (Hf)PCN-222(H_2). At a dose rate of 3.6 $e^-Å^{-2}s^{-1}$, $D_{1/2}$ for (Hf)PCN-222(H_2) was equal to an average of 254 ± 18 $e^-Å^{-2}$, whereas it increased to 376 ± 20, and 433 ± 28 $e^-Å^{-2}$ for (Hf)PCN-222(Fe)-L, and (Hf)PCN-222(Fe)-S, respectively (Table 3). When we compare the effect of the metalation element (Pd *vs.* Fe), we observe that the Fe metalated sample, (Hf)-PCN-222(Fe)-S showed higher stability, whereas (Hf)PCN-222(Fe)-L showed lower stability than the Pd metalated sample, (Hf)PCN-222(Pd), as indicated by their corresponding $D_{1/2}$ values calculated at 3.6 $e^-Å^{-2}s^{-1}$ dose rate. These measurements show that size and/or elemental differences might also affect the electron beam stabilities of MOFs.

Table 3. Calculated average half-life dose values ($D_{1/2}$, $e^-Å^{-2}$), for each sample, at respective electron dose rates ($e^-Å^{-2}s^{-1}$).

	Half-life electron doses ($D_{1/2}$, $e^-Å^{-2}$)		
	0.6 $e^-Å^{-2}s^{-1}$	1.2 $e^-Å^{-2}s^{-1}$	3.6 $e^-Å^{-2}s^{-1}$
(Zr)NU-1000		202 ± 6	
(Hf)PCN-222(H_2)	245 ± 5	242 ± 9	254 ± 18
(Hf)PCN-222(Pd)	329 ± 11	396 ± 16	400 ± 21
(Hf)PCN-222(Fe)-L			376 ± 20
(Hf)PCN-222(Fe)-S			433 ± 28

Radiolysis, the primary mechanism leading to electron beam damage in MOFs,[15,16] is a complex process. Our results indicate a remarkable enhancement in electron beam stability for metalated MOFs compared to their pristine versions (Fig. 4-5). Additionally, the overall *d*-spacing change indicates that metalated MOFs exhibited less structural alteration (~10%) at the end in comparison to the pristine MOFs (~14%). This observation could stem from the coordination bonds established between iron or palladium ions and the porphyrin linker, strengthening the Hf-carboxylate interaction by increasing the acidity of the carboxylic group.[36] This, in turn, influences the electronic structure of the porphyrin within the metalated MOF as opposed to the non-metalated ones. This

phenomenon has been demonstrated previously to enhance the catalytic capabilities of several MOFs by introducing additional Lewis acid sites.[65–69] Furthermore, we observed that due to the variability in properties such as size and elemental content during synthesis, each sample has a unique electron beam stability. Notably, all samples exhibited negligible changes in their $D_{1/2}$ with an increased dose rate. The relationship between beam sensitivity and dose rate can be either direct, inverse, or negligible.[63,64] In the case of a direct dose-rate relationship, the sensitivity rises with increasing dose rate, possibly attributed to factors such as poor electrical conductivity, charging, and heating induced by the beam. Conversely, an inverse dose-rate relationship could stem from diffusion-limited mass loss (radicals, single atoms, ionized species), precipitation, and segregation, escalating critical dose with an increasing dose rate. In our investigation, we have observed that the dose rate effect is insignificant across the studied values (0.6, 1.2, and 3.6 $e^{-}Å^{-2}s^{-1}$), consistent with the findings from prior studies on a different MOF and organic sample.[51,70] This emphasizes the limited influence of dose rate on primary damage mechanisms, such as radiolysis in our study, with the total electron dose emerging as the critical parameter.[71] This insight suggests that when considering electron tomography, selecting lower dose rates can prolong the time that can be spent on the same particle while ensuring that the cumulative dose remains below the threshold dose.

Interestingly, those Fe-based crystals with the smallest particle size (*i.e.*, (Hf)PCN-222(Fe)-S) showed the highest stability under the electron beam. However, as there are also differences in elemental composition and ratio of Fe/Hf or Pd/Hf between the metalated samples, we cannot conclusively attribute this observation solely to particle size effects. Our findings clearly demonstrate that metalation, whether with Fe or Pd and irrespective of particle size, significantly enhances electron beam stability compared to the pristine sample. Additionally, variations in synthesis parameters lead to differences in elemental composition and particle size, both of which contribute to electron beam stability.

While this study highlights the impact of metalation on the electron beam stability, further investigation is required to decouple and systematically study the specific roles of particle size and elemental composition.

High resolution imaging

Once $D_{1/2}$ is established for every sample, an estimate of the electron dose that can be applied to a specific sample can be made. To further investigate (Zr)NU-1000, (Hf)PCN-222(H_2) and its metalated version with Pd, *i.e.* (Hf)PCN-222(Pd), at high resolution, 4D-STEM experiments were performed and iCOM images were reconstructed using the riCOM[45] algorithm. The electron dose was kept below the respective $D_{1/2}$ values as calculated in the previous section. The iCOM image of (Zr)NU-1000 clearly reveals the organic linker part of the MOF, which is not visible in the virtual ABF-STEM and ADF-STEM images (Fig. 6.a, Fig. SI.33). The iCOM image of (Hf)PCN-222(H_2) also reveals Hf metal clusters and organic linkers connecting them (Fig. 6.b). The ABF-STEM and ADF-STEM images reconstructed from the 4D-STEM data set resulted in rather noisy images where it is hard to clarify local information related to the structure (Fig. SI. 34-35).

For (Hf)PCN-222(Pd) (Fig. 6.c), the Hf metal clusters of MOF, and the metalation elements (Pd) connected to the porphyrin organic linkers were successfully revealed. Additionally, as observed in all types of images—ABF, ADF, and riCOM (Figure SI.36 and Figure 6.c)—some pores appear to be filled, likely due to the presence of adsorbed gas molecules, despite the sample being under ultra-high vacuum in the microscope for an extended period. Through additional characterization results, it is shown that the (Hf)PCN-222(Pd) sample is fully metalated (details can be found in SI section 3). The organic linker and metalation elements could not be observed from conventional images such as ABF-STEM and ADF-STEM (Fig. SI. 36). On the other hand, the high-resolution iCOM image acquired from (Hf)PCN-222(Pd) (Fig. 6.c and Fig. SI.37) successfully reveals the additional metalation elements in the structure. The location of the metalation elements matches well with the theoretical model. In some regions, aperiodicity was observed (*e.g.* Fig. SI. 37-38), even though the EDX measurements from different areas on the same sample (Figures SI.15-16, Table SI.5) are in good agreement with the expected metalation. It should be noted that the observation is based on a 2D projection of a 3D-shaped MOF, and therefore, the presence of overlapping local structures, combined with the sample being relatively thick, might lead to ambiguity.[72] The observation of an aperiodic metal atom distribution, therefore highlights the importance of local characterization techniques, which should, however, be extended to 3 dimensions in the future. Moreover, we believe that the combination of 4D-STEM with cryo conditions, represents an exciting direction for further advancements in the field as it will improve the MOF stability during illumination by the electron beam.

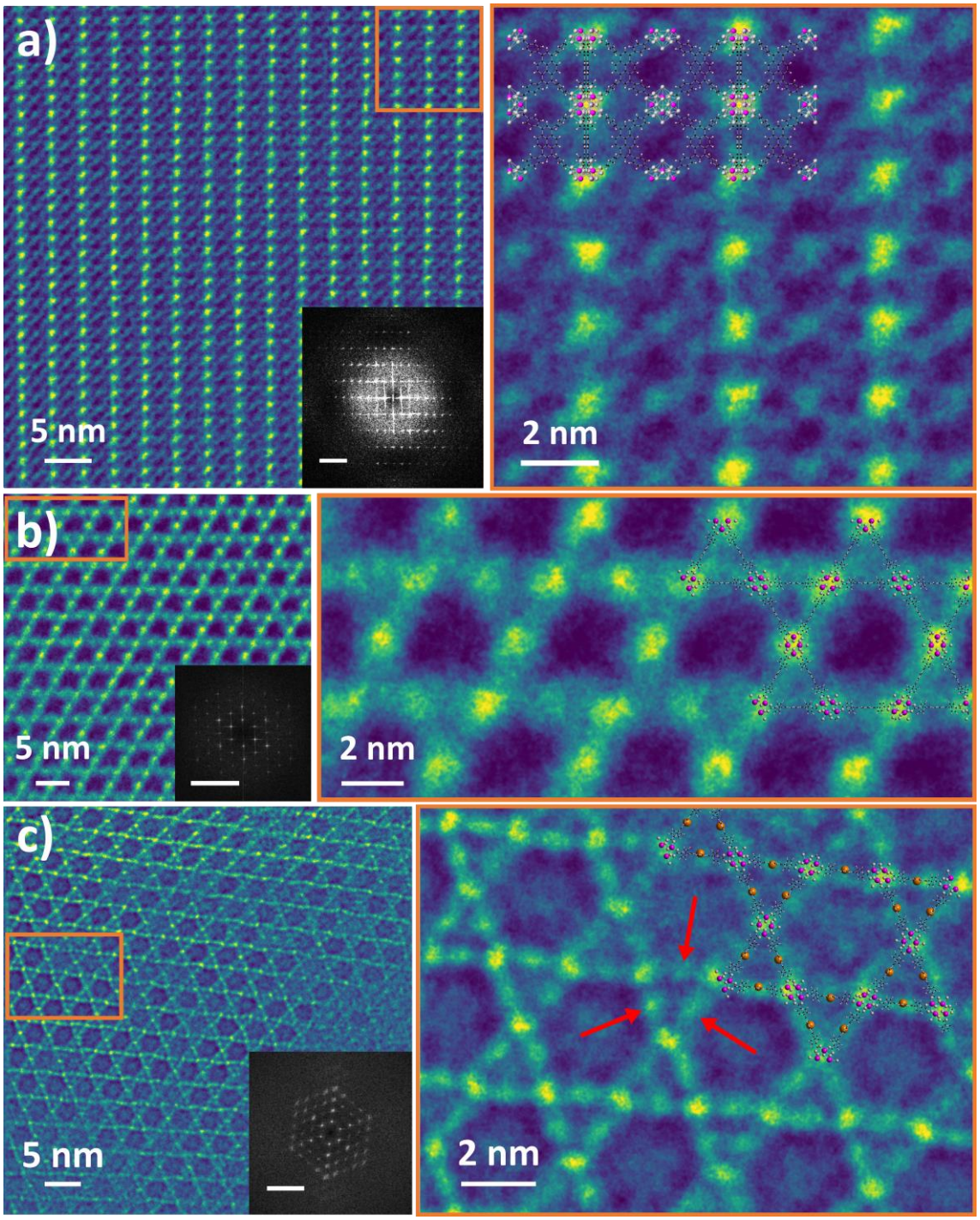

Fig. 6 High-resolution iCOM images reconstructed using riCOM algorithm from 4D-STEM data sets of (Zr)NU-1000 oriented along (100) zone axis (**a**), (Hf)PCN-222(H_2) oriented along the (001) zone axis (**b**), and (Hf)PCN-222(Pd) oriented along (001) zone axis (**c**). Insets (**a-c**) showing diffractograms of corresponding images with scale bars corresponding to 1 nm^{-1}. Magnified regions are given next to the corresponding images. Theoretical models for the structure are superimposed (Hf metals are represented by magenta spheres, displayed larger for clear visualization). Red arrows (**c**) represent the locations of metalation (Pd) elements of MOF. The 4D-STEM data sets (**a**), (**b**), and (**c**) were acquired with total electron doses of 150, 100 and 196 $e \cdot Å^{-2}$, respectively. (Please refer to section 4 in the SI for additional images).

Conclusions

In summary, our findings show that the riCOM approach is very promising to investigate the local structure of beam-sensitive materials such as MOFs at high resolution while minimizing structural alteration. For this purpose, we applied riCOM approach to metalated versions of (Hf)PCN-222(H_2) and found an unexpected local aperiodic appearance of the metalation elements. Our findings indicate the importance of evaluating the electron beam stability depending on the precise composition and size of the MOF crystals. The combination of a dedicated approach to measure the critical dose and 4D-STEM

data opens new perspectives for investigating local defects MOFs, which will eventually contribute to a better understanding of these defects in structure-property relations.

Author contributions

Safiyye Kavak: methodology, conceptualization, investigation (beam stability experiments, 4D-STEM data collection), data curation (4D-STEM data), visualization, funding acquisition, writing. Daen Jannis: supervision (4D-STEM data set acquisition), formal analysis (data quantification), writing. Annick De Backer: formal analysis (data quantification), writing. Daniel Arenas Esteban: conceptualization, writing. Arno Annys: data curation (image reconstructions), writing. Sergio Carrasco: investigation (PCN-222 MOFs synthesis and characterization), writing. Javier Ferrando-Ferrero: investigation (PCN-222 MOFs synthesis and characterization), writing. Raúl M. Guerrero: investigation (NU-1000 synthesis), writing. Patricia Horcajada: supervision (MOF synthesis), writing. Jo Verbeeck: supervision (4D-STEM data set acquisition and reconstruction), writing. Sandra Van Aert: supervision (4D-STEM data set acquisition and reconstruction), writing. Sara Bals: supervision, conceptualization, resources, funding acquisition, writing.

Conflicts of interest

There are no conflicts to declare.

Data availability

The data supporting this article have been included as part of the SI.

Acknowledgements

S.K. acknowledges the Flemish Fund for Scientific Research (FWO Vlaanderen) through a PhD research grant (Project numbers: 1181122N & 1181124N). S.B. and J.V. acknowledge the TEMPEL project (No. HBC.2021.0580) supported by Flanders Innovation Entrepreneurship (VLAIO). D.J. and J.V. acknowledge the eBEAM project supported by the European Union's Horizon 2020 research and innovation program FETPROACT-EIC-07-2020: emerging paradigms and communities, and Flemish Fund for Scientific Research (FWO Vlaanderen) with project number: G042920N ('Coincident event detection for advanced spectroscopy in transmission electron microscopy`). S.C., J.F.F and P.H. gratefully acknowledge financial support from the MICIU through the project "NAPOLION" (PID2022-139956OB-I00).

Notes and references

1 H. Furukawa, K. E. Cordova, M. O'Keeffe and O. M. Yaghi, *Science (1979)*, 2013, **341**, 1230444.
2 D. Yang and B. C. Gates, *ACS Catal*, 2019, **9**, 1779–1798.
3 A. Bavykina, N. Kolobov, I. S. Khan, J. A. Bau, A. Ramirez and J. Gascon, *Chem Rev*, 2020, **120**, 8468–8535.
4 H. Zheng, Y. Zhang, L. Liu, W. Wan, P. Guo, A. M. Nyström and X. Zou, *J Am Chem Soc*, 2016, **138**, 962–968.
5 A. E. Baumann, D. A. Burns, B. Liu and V. S. Thoi, *Commun Chem*, 2019, **2**, 86.
6 B. Li, H.-M. Wen, W. Zhou and B. Chen, *J Phys Chem Lett*, 2014, **5**, 3468–3479.
7 H. Li, K. Wang, Y. Sun, C. T. Lollar, J. Li and H.-C. Zhou, *Materials Today*, 2018, **21**, 108–121.
8 L. Liu, Z. Chen, J. Wang, D. Zhang, Y. Zhu, S. Ling, K.-W. Huang, Y. Belmabkhout, K. Adil, Y. Zhang, B. Slater, M. Eddaoudi and Y. Han, *Nat Chem*, 2019, **11**, 622–628.
9 S. Lee, S. Oh and M. Oh, *Angewandte Chemie International Edition*, 2020, **59**, 1327–1333.
10 S. Ayala, K. C. Bentz and S. M. Cohen, *Chem. Sci.*, 2019, **10**, 1746–1753.
11 H. Lai, G. Li, F. Xu and Z. Zhang, *J. Mater. Chem. C*, 2020, **8**, 2952–2963.
12 M. W. S. Chong, A. J. Parrott, D. J. Ashworth, A. J. Fletcher and A. Nordon, *Physical Chemistry Chemical Physics*, 2023, **25**, 14869–14878.
13 A. Zoubir, Ed., *Raman Imaging: Techniques and Applications*, Springer, 2012, vol. 168.
14 S. ur Rehman, S. Xu, H. Xu, T. Tao, Y. Li, Z. Yu, K. Ma, W. Xu and J. Wang, *Mater Today Adv*, 2022, **16**, 100287.
15 L. Liu, D. Zhang, Y. Zhu and Y. Han, *Commun Chem*, 2020, **3**, 99.
16 S. Ghosh, P. Kumar, S. Conrad, M. Tsapatsis and K. A. Mkhoyan, *Microscopy and Microanalysis*, 2019, **25**, 1704–1705.
17 L. Wang, M. Ma, H. Wang, H. Xiong, X. Chen, F. Wei and B. Shen, *ACS Nano*, 2023, **17**, 4740–4747.
18 Y. Li, K. Wang, W. Zhou, Y. Li, R. Vila, W. Huang, H. Wang, G. Chen, G.-H. Wu, Y. Tsao, H. Wang, R. Sinclair, W. Chiu and Y. Cui, *Matter*, 2019, **1**, 428–438.
19 J. Lv, H. Zhang, D. Zhang, L. Liu and Y. Han, *Acc Mater Res*, 2022, **3**, 552–564.
20 X. Li, J. Wang, X. Liu, L. Liu, D. Cha, X. Zheng, A. A. Yousef, K. Song, Y. Zhu, D. Zhang and Y. Han, *J Am Chem Soc*, 2019, **141**, 12021–12028.
21 D. Zhang, Y. Zhu, L. Liu, X. Ying, C.-E. Hsiung, R. Sougrat, K. Li and Y. Han, *Science (1979)*, 2018, **359**, 675–679.
22 Y. Zhu, J. Ciston, B. Zheng, X. Miao, C. Czarnik, Y. Pan, R. Sougrat, Z. Lai, C.-E. Hsiung, K. Yao, I. Pinnau, M. Pan and Y. Han, *Nat Mater*, 2017, **16**, 532–536.
23 H. Wang, L. Liu, J. Wang, C. Li, J. Hou and K. Zheng, *Molecules*, DOI:10.3390/molecules27123829.
24 M. Ma, L. Wang, H. Wang, H. Xiong, X. Chen, F. Wei and B. Shen, *Nano Lett*, 2022, **22**, 9928–9934.
25 B. Shen, X. Chen, K. Shen, H. Xiong and F. Wei, *Nat Commun*, 2020, **11**, 2692.
26 I. Lazic, E. G. T. Bosch, S. Lazar, M. Wirix and E. Yücelen, *Microscopy and Microanalysis*, 2016, **22**, 36–37.
27 K. C. Bustillo, S. E. Zeltmann, M. Chen, J. Donohue, J. Ciston, C. Ophus and A. M. Minor, *Acc Chem Res*, 2021, **54**, 2543–2551.
28 G. Li, H. Zhang and Y. Han, *ACS Cent Sci*, 2022, **8**, 1579–1588.
29 F. Haase, E. Troschke, G. Savasci, T. Banerjee, V. Duppel, S. Dörfler, M. M. J. Grundei, A. M. Burow, C. Ochsenfeld, S. Kaskel and B. V Lotsch, *Nat Commun*, 2018, **9**, 2600.
30 N. Jain, Y. Hao, U. Parekh, M. Kaltenegger, A. Pedrazo-Tardajos, R. Lazzaroni, R. Resel, Y. H. Geerts, S. Bals and S. Van Aert, *Micron*, 2023, **169**, 103444.

31 Y. Zhou, X. Xu, A. Carlsson, S. Lazar, Z. Pan, Y. Ma, O. Terasaki and H. Deng, *Chemistry of Materials*, 2020, **32**, 4966–4972.
32 R. G. Pearson, *J Am Chem Soc*, 1963, **85**, 3533–3539.
33 E.-P. Tien, G. Cao, Y. Chen, N. Clark, E. Tillotson, D.-T. Ngo, J. H. Carter, S. P. Thompson, C. C. Tang, C. S. Allen, S. Yang, M. Schröder and S. J. Haigh, *J. Mater. Chem. A*, 2024.
34 D. Mücke, I. Cooley, B. Liang, Z. Wang, S. Park, R. Dong, X. Feng, H. Qi, E. Besley and U. Kaiser, *Nano Lett*, 2024, **24**, 3014–3020.
35 D. Feng, Z.-Y. Gu, Y.-P. Chen, J. Park, Z. Wei, Y. Sun, M. Bosch, S. Yuan and H.-C. Zhou, *J Am Chem Soc*, 2014, **136**, 17714–17717.
36 D. Feng, Z.-Y. Gu, J.-R. Li, H.-L. Jiang, Z. Wei and H.-C. Zhou, *Angewandte Chemie International Edition*, 2012, **51**, 10307–10310.
37 J. Jin, *New Journal of Chemistry*, 2020, **44**, 15362–15368.
38 S. Carrasco, A. Sanz-Marco and B. Martín-Matute, *Organometallics*, 2019, **38**, 3429–3435.
39 R. Krishnan, K. Yang, K. Hashem and J. Jiang, *Molecular Catalysis*, 2022, **527**, 112407.
40 X. Jiang, F. Gou, F. Chen and H. Jing, *Green Chem.*, 2016, **18**, 3567–3576.
41 B. N. Cabral, J. L. S. Milani, A. M. Meireles, D. C. da S. Martins, S. L. da S. Ribeiro, J. S. Rebouças, C. L. Donnici and R. P. das Chagas, *New Journal of Chemistry*, 2021, **45**, 1934–1943.
42 M. Mahajan and B. Mondal, *Inorg Chem*, 2023, **62**, 5810–5821.
43 D. Bai, S. Duan, L. Hai and H. Jing, *ChemCatChem*, 2012, **4**, 1752–1758.
44 G. Cao, G. Baryshnikov, C. Chen, L. Chen, T. Zhao, S. Fu, Z. Jiang, X. Liu, Q. Li, Y. Xie and C. Li, *J Org Chem*, 2022, **87**, 9001–9010.
45 C.-P. Yu, T. Friedrich, D. Jannis, S. Van Aert and J. Verbeeck, *Microscopy and Microanalysis*, 2022, **28**, 1526–1537.
46 T. E. Webber, W.-G. Liu, S. P. Desai, C. C. Lu, D. G. Truhlar and R. L. Penn, *ACS Appl Mater Interfaces*, 2017, **9**, 39342–39346.
47 A. Bermejo-López, S. Carrasco, P. J. Tortajada, K. P. M. Kopf, A. Sanz-Marco, M. S. Hvid, N. Lock and B. Martín-Matute, *ACS Sustain Chem Eng*, 2021, **9**, 14405–14415.
48 S. Carrasco, G. Orcajo, F. Martínez, I. Imaz, S. Kavak, D. Arenas-Esteban, D. Maspoch, S. Bals, G. Calleja and P. Horcajada, *Mater Today Adv*, 2023, **19**, 100390.
49 D. Jannis, C. Hofer, C. Gao, X. Xie, A. Béché, T. J. Pennycook and J. Verbeeck, *Ultramicroscopy*, 2022, **233**, 113423.
50 F. F. Krause, M. Schowalter, O. Oppermann, D. Marquardt, K. Müller-Caspary, R. Ritz, M. Simson, H. Ryll, M. Huth, H. Soltau and A. Rosenauer, *Ultramicroscopy*, 2021, **223**, 113221.
51 Z. J. W. A. Leijten, A. D. A. Keizer, G. de With and H. Friedrich, *The Journal of Physical Chemistry C*, 2017, **121**, 10552–10561.
52 J.-Y. Tinevez, N. Perry, J. Schindelin, G. M. Hoopes, G. D. Reynolds, E. Laplantine, S. Y. Bednarek, S. L. Shorte and K. W. Eliceiri, *Methods*, 2017, **115**, 80–90.
53 D. Ershov, M.-S. Phan, J. W. Pylvänäinen, S. U. Rigaud, L. Le Blanc, A. Charles-Orszag, J. R. W. Conway, R. F. Laine, N. H. Roy, D. Bonazzi, G. Duménil, G. Jacquemet and J.-Y. Tinevez, *Nat Methods*, 2022, **19**, 829–832.
54 R. F. Egerton, *Micron*, 2019, **119**, 72–87.
55 C. Ophus, *Microscopy and Microanalysis*, 2019, **25**, 563–582.
56 T. J. Pennycook, A. R. Lupini, H. Yang, M. F. Murfitt, L. Jones and P. D. Nellist, *Ultramicroscopy*, 2015, **151**, 160–167.
57 H. Yang, T. J. Pennycook and P. D. Nellist, *Ultramicroscopy*, 2015, **151**, 232–239.
58 I. Lazić, E. G. T. Bosch and S. Lazar, *Ultramicroscopy*, 2016, **160**, 265–280.
59 D. Jannis, C. Hofer, C. Gao, X. Xie, A. Béché, T. J. Pennycook and J. Verbeeck, *Ultramicroscopy*, 2022, **233**, 113423.
60 R. F. Egerton, P. Li and M. Malac, *Micron*, 2004, **35**, 399–409.
61 L. Reimer and C. J. Arceneaux, 31. EMSA meeting, New Orleans, Louisiana, USA, 1973.
62 S. Carrasco, G. Orcajo, F. Martínez, I. Imaz, S. Kavak, D. Arenas-Esteban, D. Maspoch, S. Bals, G. Calleja and P. Horcajada, *Mater Today Adv*, 2023, **19**, 100390.
63 R. Egerton, *Micros Today*, 2021, **29**, 56–59.
64 Q. Chen, C. Dwyer, G. Sheng, C. Zhu, X. Li, C. Zheng and Y. Zhu, *Advanced Materials*, 2020, **32**, 1907619.
65 J. A. Johnson, J. Luo, X. Zhang, Y.-S. Chen, M. D. Morton, E. Echeverría, F. E. Torres and J. Zhang, *ACS Catal*, 2015, **5**, 5283–5291.
66 K. Epp, A. L. Semrau, M. Cokoja and R. A. Fischer, *ChemCatChem*, 2018, **10**, 3506–3512.
67 C. Tang, X. Li, Y. Hu, X. Du, S. Wang, B. Chen and S. Wang, *Molecules*, DOI:10.3390/molecules29020467.
68 J. Jin, *New J. Chem.*, 2020, **44**, 15362–15368.
69 A. Ebrahimi and L. Krivosudský, *Molecules*, DOI:10.3390/molecules27154917.
70 S. Ghosh, H. Yun, P. Kumar, S. Conrad, M. Tsapatsis and K. A. Mkhoyan, *Chemistry of Materials*, 2021, **33**, 5681–5689.
71 N. Jiang, *Micron*, 2023, **171**, 103482.
72 X. Peng, P. M. Pelz, Q. Zhang, P. Chen, L. Cao, Y. Zhang, H.-G. Liao, H. Zheng, C. Wang, S.-G. Sun and M. C. Scott, *Nat Commun*, 2022, **13**, 5197.